Pergamon

Int. J. Heat Mass Transfer. Vol. 38, No. 8, pp. 1377–1386, 1995

0017-9310/95 $9.50+0.00

0017-9310(94)00266-5

Propagation of condensation front in steam injection into dry porous media

K. HANAMURA† and M. KAVIANY‡

Department of Mechanical Engineering and Applied Mechanics, University of Michigan, Ann Arbor, MI 48109, U.S.A.

(*Received* 14 *April* 1994 *and in final form* 2 *August* 1994)

Abstract—The front speed and the liquid saturation distribution in the condensate flow region have been examined for one-dimensional injection of dry steam into a lower temperature, dry porous medium with a constant inlet pressure. Existing models for the volumetric viscous and inertial forces are used along with an upstream region with an immobile liquid, which is followed by a two-phase region, a condensation zone, a liquid region, and a downstream noncondensable gas flow region. The down- and upflow (along and against gravity) are examined assuming a quasi-steady behavior. For downflow, the liquid region grows with the condensation front location. The asymptotic front speed is obtained in closed form for both the near-field regime, where the steam flow rate is high (i.e. deviation from a Darcy behavior is significant), and the far-field regime. For upflow, the liquid region gradually disappears, the liquid saturation distribution in the upstream immobile region undergoes two transitions, and correlation expressions are found for the location of these transitions. An experiment is performed, and the experimental results confirm the predictions for both down- and upflows.

1. INTRODUCTION

When dry, saturated steam is injected into a dry porous medium, which is at a lower temperature, the steam condenses and the condensate may flow if the liquid saturation is larger than a threshold value needed for a continuous liquid phase (i.e. larger than an irreducible saturation s_{ir}). The flow is driven by a combination of hydrostatic, capillary and externally applied pressures and opposed by retarding forces, which are modeled by a combination of the viscous Stokes (i.e. Darcy) and inertial (i.e. Ergun-type) terms. The steam supply is through a maintained pressure source, and, therefore, as elapsed time increases and a condensate is formed within the porous medium, the inlet steam flow rate decreases. The condensate may be present as an irreducible liquid saturation in a discontinuous state, as an immobile liquid saturation with a net balance between the driving forces, as a two-phase liquid–vapor flow with a liquid saturation less than unity but larger than s_{ir}, or as a single-phase liquid flow (i.e. unity liquid saturation).

The condensate front travels at a speed that depends on the distribution of the liquid saturation in the condensate region. The prediction of the front location and the saturation distribution upstream of it requires the simultaneous evaluation of the transport (species, momentum, and thermal energy) and phase change (i.e. condensation). Because of the complexity of the analysis, generally various regions are defined within which proper simplifications can be made. Also, the commonly used empirical models (including inertial force) describing momentum conservation contain viscous terms that are of a lower differential order (as compared to the more elaborate phasic-volume averaged models that resemble the Navier–Stokes equations) and do limit the vigor of the analysis by not satisfying all the boundary conditions. However, for one-dimensional flows, such as the one considered here, significant insight and predictive ability have been obtained by using these empirical momentum equations and by defining subregions in the condensate region with jumps across them in some of the variables.

Among the previous studies, the condensation of injected steam into a liquid saturated porous medium has been studied analytically [1–4, 6–8], numerically [9], and experimentally [5–8], as related to the enhanced oil recovery and the displacement of soil contaminants. Recently, the detailed mechanisms of the steam drive processes have been studied using a two-phase region model that includes hydrostatic, capillary and external pressures, and viscous and inertial forces [6, 7]. Under the condition of a constant mass flow rate of steam, the front speed has been predicted, and the effect of the gravity direction (with respect to the flow) on the front speed has been elucidated over a wide range of system parameters [7]. In that case, the front speed remains constant, and in the two-phase region far from the front, a zero capillary pressure gradient is assumed, leading to a minimum liquid saturation.

In this study, under the condition of a constant inlet

† Permanent address: Department of Mechanical Engineering, Gifu University, Yanagido, Gifu 501-11, Japan.

‡ Author to whom correspondence should be addressed.

NOMENCLATURE

Bo	Bond number
c_p	specific heat [J kg^{-1} K^{-1}]
Ca	capillary number
C_E	Ergun coefficient
D	total axial diffusivity [m^2 s^{-1}]
g	gravitational constant [m s^{-2}]
Δi_{lg}	heat of vaporization [J kg^{-1}]
Ja	Jakob number
K	absolute permeability [m^2]
k	conductivity [W m^{-1} K^{-1}]
k_e	effective conductivity [W m^{-1} K^{-1}]
K_r	relative permeability
$\dot{n}$	volumetric rate of production [s^{-1}]
p	pressure [Pa]
p_c	capillary pressure [Pa]
Pe_l	liquid Péclet number
R	radius of glass particle
Re	Reynolds number
s	liquid saturation
s_{im}	immobile liquid saturation
s_{ir}	irreducible liquid saturation
S	scaled liquid saturation
S_c	critical scaled liquid saturation
t	time [s]
T	temperature [K]
u	superficial velocity [m s^{-1}]
u_F	condensation front velocity [m s^{-1}]
x	axial location [m].

Greek symbols

α_l	liquid diffusivity [m^2 s^{-1}]
δ_l	thickness of liquid region [m]
δ_{lg}	thickness of two-phase region [m]
ε	porosity
μ	viscosity [kg m^{-1} s^{-1}]
ρ	density [kg m^{-3}]
σ	surface tension [N m^{-1}].

Subscripts

a	air
e	exit
F	front
g	gas
i	initial
ir	irreducible
l	liquid
m	modified
s	solid
sat	thermodynamic saturation state
tr	transition
0	inlet
1	first
2	second.

Superscript

*	dimensionless.

pressure, the propagation of the condensation front into a dry porous medium is investigated theoretically both for downward and upward flows (relative to gravity). The saturation distribution within various predicted regions is examined and some closed-form and appropriate solutions for the front speed are found. Experiments are also performed using a packed column of spherical glass particles with down- and upflow of steam, with the results compared with those predicted.

2. ANALYSIS

Steam and condensate displace the noncondensable gas initially occupying the pore space. Based on experimental observations, an analysis of the phase change and two-phase flow will be made by defining various regions over which appropriate approximations are made. In the following, first a physical model for the phase change and two-phase flow is given. Then, the conservation equations and boundary conditions for each region are discussed and finally the required numerical integration is described.

2.1. *Physical model*

Figure 1 shows the model used for the downflow of steam with the anticipated axial distributions of the temperature, pressure and liquid saturation within the various defined regions. The porous medium is initially dry, i.e. the pore space is filled with air at a temperature T_i, lower than the saturation temperature T_{sat} (at atmospheric pressure). Four different regions are defined, namely, the upstream, followed by two-phase, liquid and downstream regions. The inlet pressure is p_0, and the inlet thermodynamic quality is assumed unity. Steam condensation is assumed to occur at the condensation zone (of a negligibly small thickness) x_F located between the liquid and two-phase regions. In the liquid region, the liquid saturation is assumed as unity. In the two-phase region, the liquid saturation varies, both phases are mobile, and the capillary pressure is nonzero. No liquid motion is allowed in the upstream region. Although the condensation-front speed is not constant, under the condition of a constant inlet pressure, a quasi-steady state behavior is assumed through all the regions. This is justifiable when the change in front speed is small with respect to time and will be discussed later. The volumetric viscous force for the flow is described by Darcy's law along with a deviation, which is the microscopic inertial force (the Ergun inertial term). The relative permeabilities in the viscous and inertial terms are prescribed functions of the scaled and absolute liquid saturations, respectively.

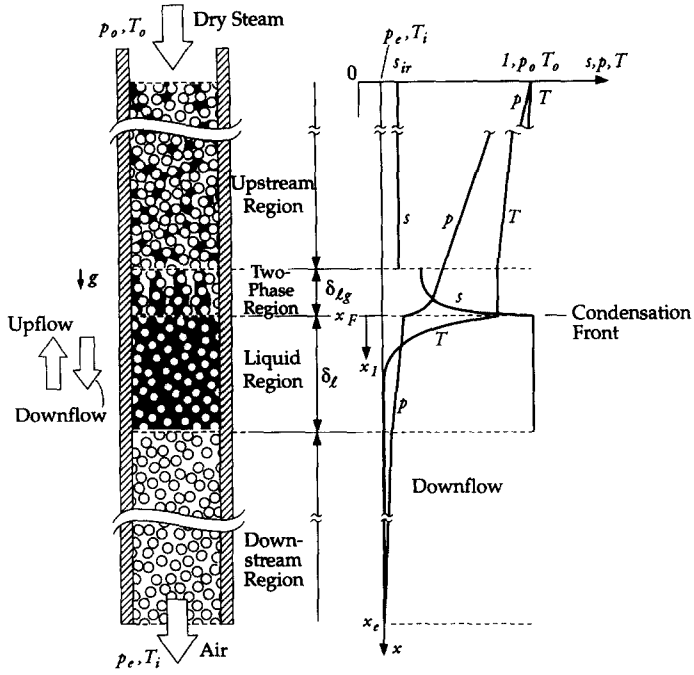

Fig. 1. Anticipated axial distributions of the temperature, pressure and liquid saturation, and a rendering of the various regions along the packed column (for the downflow).

Furthermore, the gas, liquid and solid phases are assumed to be in local thermal equilibrium. The front is assumed to be stable and physical properties are assumed constant.

2.2. *Governing equations*

The dimensionless, two-phase flow conservation equations for the liquid- and gas-phase mass and momentum, and for the thermal energy (under the assumption of local thermal equilibrium) are [10]:

$$\varepsilon Bo\frac{\partial s}{\partial t^*}+\frac{\partial Ca_l}{\partial x^*}=\dot{n}_l^* \tag{1}$$

$$-\varepsilon Bo\frac{\partial s}{\partial t^*}+\mu^*\frac{\partial Ca_g}{\partial x^*}=\dot{n}_g^* \tag{2}$$

$$\frac{\partial p_l^*}{\partial x^*}=\frac{Bo_l}{Bo}-\frac{Ca_l}{Bo}\left(\frac{1}{K_{rl}}+\frac{C_E Re_l}{K_{rli}}\right) \tag{3}$$

$$\frac{\partial p_g^*}{\partial x^*}=\frac{Bo_g}{Bo}-\frac{Ca_g}{Bo}\left(\frac{1}{K_{rg}}+\frac{C_E Re_g}{K_{rgi}}\right) \tag{4}$$

$$K_{rl}=S^3 \quad K_{rg}=(1-S)^3 \quad S=\frac{s-s_{ir}}{1-s_{ir}} \tag{5}$$

$$K_{rli}=s^6 \quad K_{rgi}=(1-s)^6 \tag{6}$$

$$[(1-\varepsilon)+\varepsilon s(\rho c_p)_l^*+\varepsilon(1-s)(\rho c_p)_g^*]Bo\frac{\partial T^*}{\partial t^*}$$
$$+[sCa_l(\rho c_p)_l^*+(1-s)Ca_g(\rho c_p)_g^*\mu^*]\frac{\partial T^*}{\partial x^*}$$
$$=\left[s+(1-s)(\rho c_p)_{gl}^*\frac{D_g}{D_l}\right](\rho c_p)_l^*\frac{Bo}{(Pe_l)_m}\frac{\partial^2 T^*}{\partial x^{*2}}+\frac{\dot{n}_l^*}{Ja} \tag{7}$$

where the normalized length, time, temperature, and pressure and the dimensionless parameters are

$$x^*=\frac{xBo}{(K\varepsilon)^{1/2}}, \quad t^*=\frac{tBo^2\sigma}{(K\varepsilon)^{1/2}\mu_l} \tag{8}$$

$$T^*=\frac{T-T_i}{T_{F,sat}-T_i}=\frac{T-T_i}{\Delta T} \tag{9}$$

$$p_l^*=\frac{p_l-p_e}{\sigma}\left(\frac{K}{\varepsilon}\right)^{1/2} \quad p_g^*=\frac{p_g-p_e}{\sigma}\left(\frac{K}{\varepsilon}\right)^{1/2} \tag{10}$$

$$Ca_l=\frac{\mu_l u_l}{\sigma} \quad Ca_g=\frac{\mu_g u_g}{\sigma} \tag{11}$$

$$Re_l=\frac{\rho_l u_l K^{1/2}}{\mu_l} \quad Re_g=\frac{\rho_g u_g K^{1/2}}{\mu_g} \tag{12}$$

$$Bo=\frac{(\rho_l-\rho_g)gK}{\sigma} \quad Bo_l=\frac{\rho_l gK}{\sigma}$$

$$Bo_g=\frac{\rho_g gK}{\sigma} \quad \rho^*=\frac{\rho_g}{\rho_l} \tag{13}$$

$$(\rho c_p)_l^*=\frac{(\rho c_p)_l}{(\rho c_p)_s} \quad (\rho c_p)_g^*=\frac{(\rho c_p)_g}{(\rho c_p)_s} \quad (\rho c_p)_{gl}^*=\frac{(\rho c_p)_g}{(\rho c_p)_l} \tag{14}$$

$$\mu^*=\frac{\mu_l}{\mu_g} \quad (Pe_l)_m=\frac{(K\varepsilon)^{1/2}\sigma}{D_l\mu_l} \quad Ja=\frac{c_{pl}\Delta T}{\Delta i_{lg}}\frac{1}{(\rho c_p)_l^*}. \tag{15}$$

The scaled liquid saturation S is defined in equation (5). The modified Péclet number $(Pe_l)_m$ is based on the total axial diffusivity and the square root of the

absolute permeability, and ΔT is the difference between the initial temperature and the saturation temperature evaluated at front pressure. For the upflows, the sign of the gravity term is changed.

Upstream region, $0 \leqslant x^* \leqslant x_F^* - \delta_{lg}^*$. In this region the liquid remains in the pores after the passing of the front and is considered immobile; no phase change occurs and the capillary pressure is assumed constant. Then we have

$$\dot{n}_l^* = \dot{n}_g^* = 0, \quad u_l = 0 \text{ (i.e. } Ca_l = 0)$$

$$u_g = u_{g,0} \text{ (i.e. } Ca_g = Ca_{g,0})$$

$$p_c^* = p_g^* - p_l^* = \text{constant}, \quad T^* = T_{sat}^*(p_g). \quad (16)$$

Since $p_c^* = p_g^* - p_l^*$ is constant, subtracting equation (3) from equation (4) will produce

$$\frac{\partial p_c^*}{\partial x^*} = -1 - \frac{Ca_{g,0}}{Bo}\left(\frac{1}{K_{rg}} + \frac{C_E Re_{g,0}}{K_{rgi}}\right) = 0 \quad (s \geqslant s_{ir}). \quad (17)$$

Equation (17) is used to determine the continuous but immobile liquid saturation $s_{im} = s_{im}(x^*)$, and, as evident, this distribution depends on the ratio of the Bond and capillary numbers. When there does not exist a real positive solution for s_{im}, then it is assumed that $s_{im} = s_{ir}$. As will be shown, this is the case for the downflow. However, for the upflow s_{im} varies with x^* starting from s_{ir} at the first transition point $x_{tr,1}^*$ and increasing monotonically until the second transition point $x_{tr,2}^*$. Further, the saturation gradient (i.e. the capillary pressure gradient) is negligibly small.

Two-phase region, $x_F^* - \delta_{lg}^* \leqslant x^* \leqslant x_F^*$. In this region, both the liquid and vapor are mobile, and no phase change occurs:

$$\dot{n}_l^* = \dot{n}_g^* = 0 \quad T^* = 1. \quad (18)$$

The propagation velocity of the condensation front can be regarded as the pore velocity of the liquid at the front. Using a moving coordinate system based on the condensation-front speed, i.e. $x_l^* = x^* - (u_F^*/Bo)t^*$ (where $u_F^* = u_F \mu_l/\sigma$), equations (1) and (2) are rewritten as

$$\frac{\partial}{\partial x_l^*}(Ca_l - \varepsilon s u_F^*) = 0 \quad (19)$$

$$\frac{\partial}{\partial x_l^*}(\mu^* Ca_g + \varepsilon s u_F^*) = 0. \quad (20)$$

Using $Ca_l = \varepsilon u_F^*$ (i.e. $u_l = \varepsilon u_F$) and $\mu^* Ca_g = \mu^* Ca_{g,0} - \varepsilon u_F^*$ (i.e. $u_g = u_{g,0} - \varepsilon u_F$) at the front, where $s = 1$, the solutions to the above equations are

$$Ca_l = \varepsilon u_F^* \quad (21)$$

$$\mu^* Ca_g = \mu^* Ca_{g,0} - \varepsilon u_F^*. \quad (22)$$

Writing the capillary pressure in terms of the Leverett J-function, the liquid saturation distribution is determined from the following equation, which is derived by subtracting equation (3) from equation (4):

$$\frac{\partial S}{\partial x_l^*} = \frac{\dfrac{Ca_g}{Bo}\left[\left(\dfrac{1}{K_{rg}} + \dfrac{C_E Re_g}{K_{rgi}}\right) - \dfrac{Ca_l}{Ca_g}\left(\dfrac{1}{K_{rl}} + \dfrac{C_E Re_l}{K_{rli}}\right) + \dfrac{Bo}{Ca_g}\right]}{\left(\dfrac{dJ(S)}{dS}\right)}. \quad (23)$$

where

$$p_c^* = \frac{p_c}{\sigma}\left(\frac{K}{\varepsilon}\right)^{1/2} = J(S) \quad (24)$$

$$J(S) = 1.417(1-S) - 2.120(1-S)^2 + 1.263(1-S)^3. \quad (25)$$

The boundary condition for the scaled liquid saturation is $S = 1$ at the condensation front.

In the two-phase region the scaled liquid saturation increases monotonically from S_c at $x_l^* = -\delta_{lg}^*$ to $S = 1$ at the front, where S_c (as discussed in ref. [7]) is the critical liquid saturation and is obtained by imposing the condition of a zero liquid saturation gradient, i.e. $dS/dx_l^* = 0$. This corresponds to setting the numerator of equation (23) equal to zero. In the second term in the numerator, the relative permeabilities K_{rl} and K_{rli} are proportional to the third and sixth powers of liquid saturation, respectively, while the liquid velocity u_l (i.e. Ca_l) is proportional to the first power of the liquid saturation. Since the magnitude of the second term in equation (23) increases with a decrease in the liquid saturation, the magnitude of the critical absolute liquid saturation is always greater than s_{ir}.

Condensation front, $x^* = x_F^*$. At the front, the energy released due to phase change is transferred to the condensed liquid, i.e.

$$-\frac{Bo}{(Pe_l)_m} Ja(\rho c_p)_l^* \left.\frac{\partial T^*}{\partial x_l^*}\right|_{x_l^* = 0^-} = \rho^*(\mu^* Ca_{g,0} - \varepsilon u_F^*). \quad (26)$$

Through the integration of equation (32) given below, this heat flux is also given through

$$(1-\varepsilon)u_F^* - \varepsilon(\rho c_p)_l^* \Delta Ca_l = -\frac{Bo}{(Pe_l)_m}(\rho c_p)_l^* \left.\frac{\partial T^*}{\partial x_l^*}\right|_{x_l^* = 0^-}. \quad (27)$$

The second term on the left-hand side of equation (27) represents the sensible heat of the condensed liquid: ΔCa_l is determined from equation (31) below. Then $Ca_{g,0}$ (i.e. $u_{g,0}$) is determined from equations (26) and (27), which give

$$\rho^*(\mu^* Ca_{g,0} - \varepsilon u_F^*) = Ja[(1-\varepsilon)u_F^* - \varepsilon(\rho c_p)_l^* \Delta Ca_l]. \quad (28)$$

Liquid region, $x_F^* \leqslant x^* \leqslant x_F^* + \delta_l^*$. In the liquid

region the porous medium is completely saturated with the subcooled liquid, and we have

$$s = 1, \quad \dot{n}_l^* = \dot{n}_g^* = 0, \quad \mu_l = \mu_{l,i}. \tag{29}$$

The thickness of the liquid region δ_l^*, which begins at x_F^*, is determined from the total mass balance and is

$$\delta_l^* = Ja\, x_F^* \frac{1-\varepsilon}{\varepsilon} - \int_0^{x_F^*} s\, dx^*. \tag{30}$$

The pore liquid velocity is the sum of the front velocity and the rate of increase in the thickness of the liquid region. Then, the superficial velocity u_l (i.e. Ca_l) and ΔCa_l are determined from

$$Ca_l = \varepsilon(u_F^* + \Delta Ca_l) = \varepsilon\left(u_F^* + \frac{\partial \delta_l^*}{\partial t^*}\right)$$

$$= \varepsilon u_F^*\left(1 + Ja\frac{1-\varepsilon}{\varepsilon} - \frac{1}{u_F^*}\frac{\partial}{\partial t^*}\int_0^{x_F^*} s\, dx^*\right). \tag{31}$$

The energy equation is also transformed to the moving coordinate system and gives

$$\{-[(1-\varepsilon)+\varepsilon(\rho c_p)_l^*]u_F^*$$

$$+ (\rho c_p)_l^* Ca_l\}\frac{\partial T^*}{\partial x_l^*} = (\rho c_p)_l^* \frac{Bo}{(Pe_l)_m}\frac{\partial^2 T^*}{\partial x_l^{*2}}. \tag{32}$$

Integrating this for $0 \leqslant x^* \leqslant \infty$ and using the zero gradient conditions in the far-field gives equation (27). The solution to equation (32), subject to the boundary conditions $T^* = 1$ at $x_l^* = 0$ and $T^* \to 0$ as $x_l^* \to \infty$, is

$$T^* = \exp\left\{-(Pe_l)_m\left[(1-\varepsilon)+\varepsilon(\rho c_p)_l^*\right.\right.$$

$$\left.\left.\times\left(Ja\frac{1-\varepsilon}{\varepsilon} - \frac{1}{u_F^*}\frac{\partial}{\partial t^*}\int_0^{x_F^*} s\, dx^*\right)\right]\frac{u_F^* x_l^*}{Bo}\right\}. \tag{33}$$

The total axial diffusivity D_l is related to the liquid Péclet number Pe_l and the effective conductivity k_e through the empirical relation [10, 11]:

$$\frac{D_l}{\alpha_l} = \frac{k_e}{k_l} + 0.5 Pe_l \quad Pe_l = \frac{u_l R}{\alpha_l} \tag{34}$$

where α_l is the thermal diffusivity of the liquid and R is the radius of the particle. The effective conductivity used is the empirical relation of Krupiczka [10, 12].

Downstream region, $x_F^* + \delta_l^* \leqslant x^* \leqslant x_e^*$. There is no liquid in the downstream region, and at $x^* = x_F^* + \delta_l^*$ the gas velocity is assumed to be equal to the liquid velocity. This region is described by

$$\dot{n}_g^* = 0 \quad u_g = u_l(x^* = x_F^* + \delta_l^*)$$

$$(\text{i.e. } Ca_g = Ca_l) \quad K_{rg} = K_{rgi} = 1$$

$$p_g^*(x_F^* + \delta_l^*) = p_l^*(x_F^* + \delta_l^*)$$

$$(\text{i.e. no meniscus-curvature effect}) \ \mu_g = \mu_a, \rho_g = \rho_a. \tag{35}$$

2.3. *Numerical integration*

Since the front speed u_F is not known *a priori* and the thermal and hydrodynamic aspects of the problem are nonlinear and coupled, u_F is obtained by a numerical iteration. At a front location $0 \leqslant x_F^* \leqslant x_e^*$, first a guessed value of u_F^* is used and then the scaled liquid saturation in the upstream region just behind the two-phase region is obtained from equation (17). As mentioned before, when no real positive solution exists, the absolute value of the liquid saturation is taken as s_{ir}. The scaled critical liquid saturation S_c is then determined from setting the liquid saturation gradient equal to zero in equation (23) with Ca_l (i.e. u_l) and Ca_g (i.e. u_g) from equations (21) and (22). Among the roots, the largest value of S_c is used. Then, using this S_c as the initial guess, equation (23) is numerically integrated using the Runge–Kutta method along x_l^* until the liquid saturation reaches the value of unity. To avoid problems associated with numerical truncations, a value just slightly larger than S_c is used in the initial-value numerical integration. The region behind the front, from the location where $(1-S)/(1-S_c) = 0.99$ to the location where $S = 1$, is defined as the two-phase region. In the liquid and the downstream regions, the absolute liquid saturations are equal to unity and zero [except we use $K_{rg} = (1-S)^3 = 1$ in the downstream region], respectively. The relative permeabilities in each region are determined from the liquid saturation distributions. Further, the liquid- and gas-phase velocities, u_l (i.e. Ca_l), and u_g and $u_{g,0}$ (i.e. Ca_g and $Ca_{g,0}$), are found in terms of the condensation-front speed u_F^* through equations (21), (22), (28) and (31). Then, the value of u_F^* is updated, solving equations (3) and (4) using the boundary conditions $p^* = p_0^*$ at the inlet and $p^* = 0$ at the exit. Note that, in order to avoid the singularity at the front, where $S = 1$, equation (4) is integrated up to the location where $S = 0.95$. The convergence criterion for u_F^* is taken as the difference in its magnitude between any two successive iterations, and a converged solution is found when this is less than 1% of the current magnitude of u_F. Using the converged u_F^* and the saturation distributions, the temperature distribution in the liquid region is obtained from equation (33).

The absolute permeability is estimated from the Carman–Kozeny equation, and the thermophysical properties used are listed in Table 1. In comparing the

Table 1. Thermophysical properties used in computations [13]

C_E	0.55	μ_l	0.28×10^{-3} N s m^{-2}
c_{pl}	4186 J kg^{-1} K^{-1}	$\mu_{l,i}$	0.96×10^{-3} N s m^{-2}
K	3×10^{-10} m^2	μ_a	1.85×10^{-5} N s m^{-2}
k_l	0.656 W m^{-1}	ρ_a	1.16 kg m^{-3}
Δi_{lg}	2.257×10^6 J kg^{-1}	ρ_g	0.6 kg m^{-3}
R	250 μm	ρ_l	958 kg m^{-3}
ΔT	80 K	$(\rho c_p)_s$	3.149×10^6 J m^{-3} K^{-1}
ε	0.40	σ	0.0589 N m^{-1}
μ_g	1.2×10^{-5} N s m^{-2}		

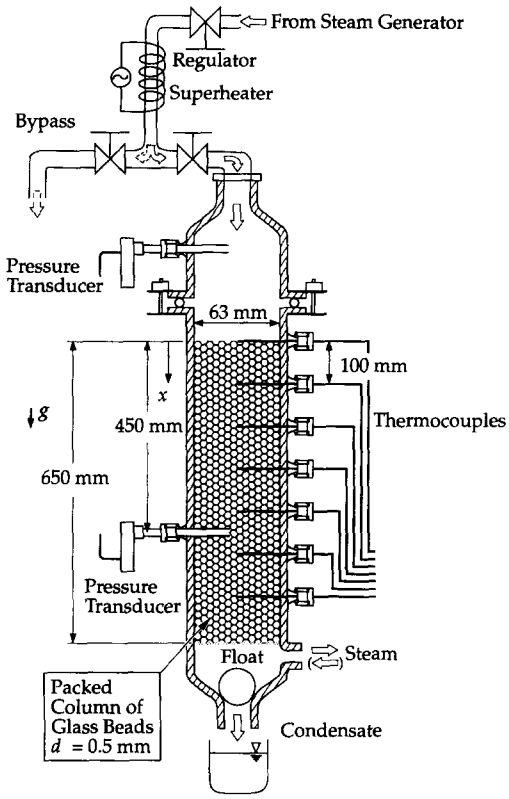

Fig. 2. A schematic of the experiment showing the downward steam flow, the upstream superheater, the location of pressure transducers and thermocouples, and the downstream phase separator. For upward steam flow the upstream superheater and other accessories are moved to the bottom of the packed column.

prediction with the experimental results, the volumetric heat capacity of the packed bed is modified by including the volumetric heat capacity of the containing glass tube. This is done multiplying the former by a factor of 1.64, which is obtained from the volume averaging.

3. EXPERIMENT

Spherical glass particles with an average diameter of 500 μm are packed in a Pyrex tube of 63 mm inner diameter, 76.2 mm outer diameter, and 650 mm length. A schematic of the experiment for the downflow of steam is shown in Fig. 2. Temperature is measured every 100 mm along the axis and at the center of the bed using thermocouples. The average propagation speed of the condensation front u_F is determined from the elapsed time measured for the travel of the front (marked by a prescribed temperature between T_i and T_{sat}) between adjacent thermocouples. At 400 mm from the entrance, the temperature is also measured at one-half the distance between the center and the surface to verify the one-dimensionality of the front. The pressure is measured by transducers, one located at the top of the column and another further downstream, and the pressure history at these locations is recorded.

In order to prevent any condensation prior to arrival into the packed bed, the steam from the generator is flown through the bypass line (as shown in Fig. 2). The steam is then superheated using a heater to about 10 K above the saturation temperature (at the inlet pressure). Then, this steam is flown to the packed column such that at the entrance it is close to the saturated state. The condensate flow is measured at the column exit, and the flow of dry air is used for a complete drying of the column at the end of each experiment.

Both, the down- and upward steam flows are considered in order to examine the effect of gravity on the front structure and the propagation speed. For the upflow, the superheater and other accessories are placed at the bottom of the column. In order to estimate the heat losses from the glass tube, the experiments are performed with and without an insulator placed on the tube.

The porosity of the bed is determined using the tube inner volume, the mass of the glass particles, and their density. The porosity is also measured by a nearly complete saturation with water and a very close agreement is found, i.e. the irreducible nonwetting-phase saturation $s_{ir,g}$, is negligibly small. The irreducible wetting-phase saturation s_{ir} is measured using a packed column consisting of a stainless steel tube of 25 mm inner diameter and 600 mm length and the same glass particles. The measured value, $s_{ir} = 0.1$, is accurate to within 10%.

4. RESULTS AND DISCUSSION

For the downflow of steam, the predicted axial pressure distribution (for three different front locations) is shown in Fig. 3. The predicted thicknesses of the two-phase and liquid regions, δ_{lg}^* and δ_l^*, are also depicted. Note that the front speed decreases

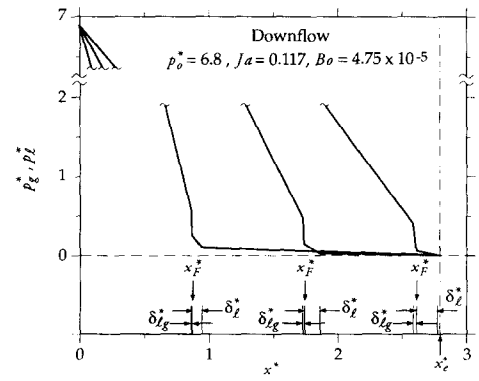

Fig. 3. Predicted scaled axial pressure distribution for three different front locations. The predicted thicknesses of the two-phase and liquid regions are also shown. The results are for the downflow and $p_0^* = 6.8$.

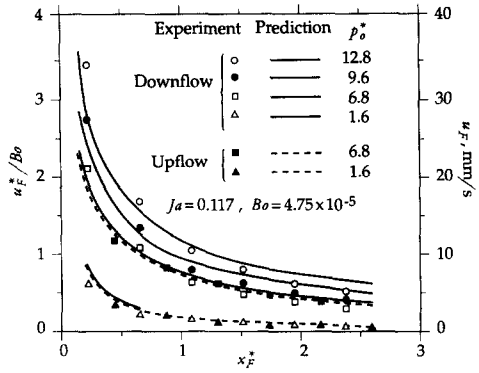

Fig. 4. Predicted and measured variations of the dimensional and normalized front speed with respect to the scaled front location for the up- and downflow and for several inlet pressures.

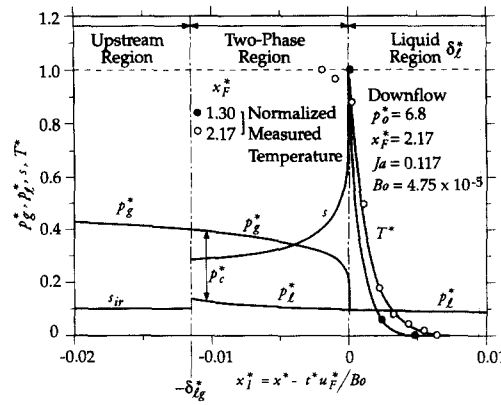

Fig. 5. Predicted axial (in the moving coordinate x_l^*) distributions of the normalized temperature, liquid saturation, and gas- and liquid-phase pressures. The results are for the downflow and $x_F^* = 2.17$. The results for the temperature at $x_F^* = 1.30$ are also included.

monotonically with x_F^*. This is evident in Fig. 4, where the predicted and measured variations of u_F^* are shown with respect to x_F^* for both the down- and upflow and for several inlet pressures. As shown in Fig. 3, for $p_0^* = 6.8$ the pressure drops significantly within the upstream region, where the vapor flow velocity $u_{g,0}$ is approximately 110 times larger than u_F. The results are for $Ja = 0.117$, corresponding to the experimental condition. In the two-phase region, $-\partial p_g^*/\partial x^*$ is larger than that in the upstream region. However, because $\delta_{lg}^* < x_F^*$ for the conditions shown, the corresponding pressure drop is much smaller. As a result, u_F^* is mainly determined by the pressure drop within the upstream region. With this pressure drop increasing, $Ca_{g,0}$ (i.e. $u_{g,0}$) and u_F^* decrease as x_F^* increases. Further, the thicknesses of the two-phase and liquid regions increase with x_F^* (the pressure drops in these regions have only a secondary effect on u_F^*). Consequently, as observed in Fig. 4, u_F^* decreases with increasing distance from the entrance under the condition of a constant inlet pressure. Over a wide range of inlet pressures, the experimental results are in good agreement with the predictions (even for small x_F^*, where u_F^* changes significantly). For the downflow and $p_0^* = 1.6$, the predicted results for $0.52 < x_F^* < x_c^*$ are not shown, because in the liquid region the gravity force exceeds the sum of the viscous and inertial forces in equation (3) and the liquid flow is expected to become unstable. In the experiments, a fingering liquid flow (with the fingers having a velocity higher than the front speed) is observed in front of a thin liquid region. However, in all the experiments, the condensation front appears as one-dimensional. Since the enthalpy of the steam flow is much larger than the heat loss to the tube periphery, the effect of this heat loss on u_F^* is negligibly small.

Figure 5 shows some typical distributions of the temperature, liquid saturation, and pressure (gas- and liquid-phase) around the condensation front, where the abscissa is the moving coordinate x_l^*. The numerical results for this front structure are for a downflow, $x_F^* = 2.17$, and $p_0^* = 6.8$. The temperature distribution for the same condition, but for $x_F^* = 1.30$, is also depicted. The normalized temperature, normalized using the initial temperature and the saturation temperature at the front, drops rapidly within a short distance in the liquid region. Note that the measured temperature is averaged over the width of the thermocouple junction (diameter of about 0.5 mm). A good agreement is found between the experimental and numerical results. The spatial origin in the experimental results is adjusted to follow the numerical results in the liquid region, because, due to the small pressure variations around the front, the exact front location cannot be determined experimentally. A direct comparison between the experimental and numerical results is not made for the case x_F^* approaching zero, because the front speed is too large for an accurate transient measurement of temperature. Note that a quasi-steady propagation is assumed. In the transformation to the moving coordinate system, the variation of u_F^* with time can be included as

$$\frac{\partial x_l^*}{\partial x^*} = 1 - \frac{\partial u_F^*}{\partial x^*}\frac{t^*}{Bo}\frac{\partial x_l^*}{\partial t^*} = -\frac{u_F^*}{Bo} - \frac{\partial u_F^*}{\partial t^*}\frac{t^*}{Bo}. \qquad (36)$$

The difference between the spatial temperature distributions obtained with and without this variation is only about 10% (at most). This close agreement between the experimental and predicted results indicates that the assumption of a quasi-steady state behavior at any front location is rather justifiable. For the downflow, equation (17) has no real positive solutions (for any ratio of Bo to $Ca_{g,0}$). In the two-phase region, the absolute liquid saturation increases sharply from that close to the critical liquid saturation to unity. As mentioned in Section 2.2, the second term on the right-hand side of equation (23) increases with a decrease in liquid saturation. As a result, the critical liquid saturation is not equal to the irreducible liquid saturation, i.e. there is a saturation jump at the beginning of the two-phase region. As the liquid saturation

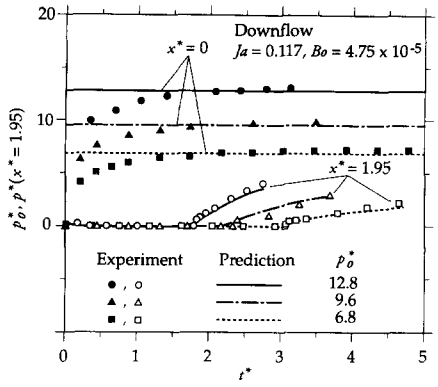

Fig. 6. Pressure histories at the entrance $x_F^* = 0$ and at $x^* = 1.95$ (distance into the packed column). The results are for the downflow and for three different inlet pressures.

increases, the gas-phase pressure drastically decreases along the flow direction. The liquid-phase pressure is lower than the gas-phase pressure by the magnitude of the capillary pressure p_c^*.

Figure 6 shows the pressure history at the entrance ($x^* = 0$) and at $x^* = 1.95$ for the downflow and for three different inlet pressures. The normalized pressure at $x^* = 1.95$ is nearly equal to zero as the downstream region passes. As the liquid region passes through $x^* = 1.95$, the predicted pressure increases almost linearly with time. The experimental results do not clearly show such a linear pressure rise. The pressure rises rapidly after the passing of the front. A similar pressure rise is found as the two-phase region passes. After the two-phase region, the upstream region passes, where the pressure also rises with respect to time. A good agreement is found between the predicted and experimental results. Note that the asymptote for $x \neq 0$ will be $p^*(x^*, t^* \to \infty) = p_0^*$. Although initially the inlet pressure in the experiments is lower and varies with time as compared to that assumed in the analysis, the measured u_F^* is in a good agreement with predictions, as shown in Fig. 4.

Figure 7 shows the predicted axial distribution of the liquid saturation for various front locations and for the upflow with $p_0^* = 1.6$. Figure 8 shows the predicted axial variation of the thickness of the liquid and two-phase regions, δ_l^* and δ_{lg}^*, for both the up- and downflow and for several inlet pressures. The measured variation δ_l^* for the downflow and $p_0^* = 6.8$ is also shown. For the downflow, the liquid saturation in the upstream region is constant, i.e. $s = s_{ir}$, as shown in Fig. 5. As a result, δ_l^* increases almost linearly with x_F^*, as shown in Fig. 8. The predicted δ_l^* for $p_0^* = 6.8$ is in good agreement with the experimental results (obtained through visual observations and by measurement of the accumulated amount of the condensate flow). For the upflow, the liquid saturation in the upstream region is maintained at s_{ir} for u_F^*/Bo higher than a critical velocity (equal to 0.177), which occurs at a location referred to as the first (i.e. the discontinuous irreducible to continuous immobile liquid saturation) transition and corresponds to

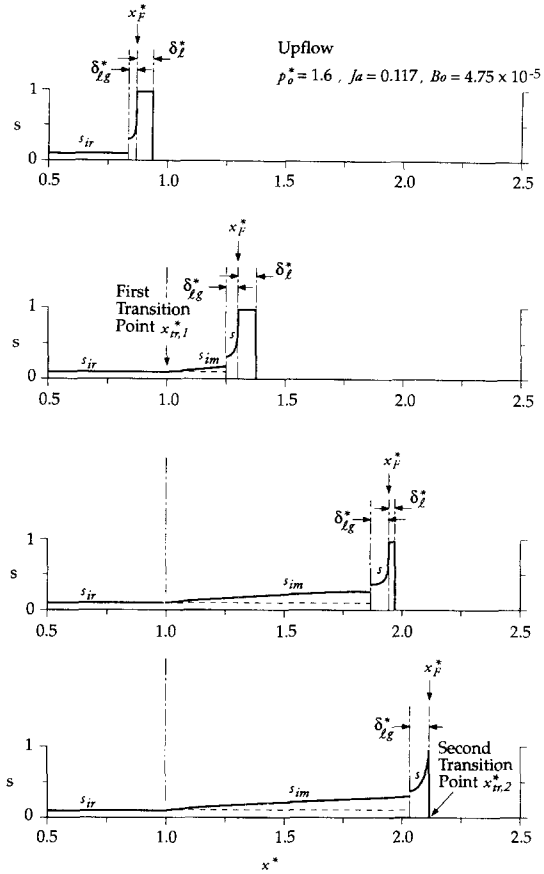

Fig. 7. Predicted axial distributions of the liquid saturation for the upflow and for various front locations. The results are for $p_0^* = 1.6$.

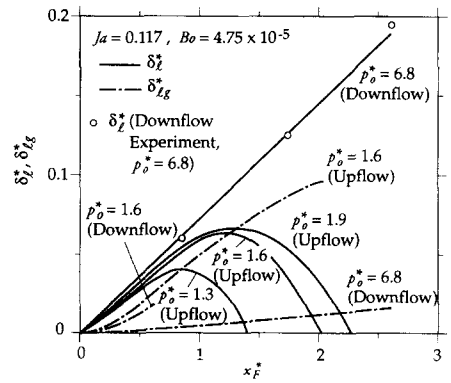

Fig. 8. Predicted axial variation of the thicknesses of the liquid and two-phase regions for the up- and downflow and for several inlet pressures. The measured variation of the thickness of the liquid region for the downflow and $p_0^* = 6.8$ is also shown.

$Bo/Ca_{g,0} = 1.18$. As shown in Fig. 9, $Bo/Ca_{g,0}$, which is independent of Ja, increases with Bo, because of the increase in the significance of the inertial term. As $Bo \to 0$, the asymptote will be $Bo/Ca_{g,0} = 1$. After the front passes through this first transition point $x_{tr,1}^*$, the liquid saturation in the upstream region begins to increase with increase in x_F^*. This saturation distri-

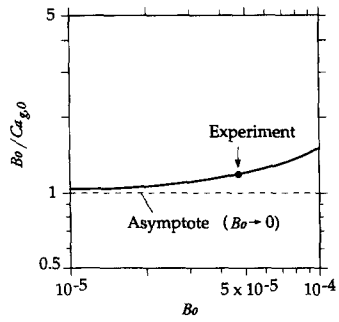

Fig. 9. Predicted critical ratio of Bo to $Ca_{g,0}$, marking the transition from a discontinuous irreducible to a continuous immobile liquid saturation.

bution, $s_{im} = s_{im}(x_F^*)$, is determined from the balance between the gravity force and the sum of the viscous and inertial forces in equation (17). Then, as shown in Fig. 8, the thickness of the liquid region begins to decrease and eventually the liquid region disappears at a location referred to as the second transition $x_{tr,2}^*$ (where $\delta_l^* = 0$). The numerical integration is halted at $x_{tr,2}^*$. Therefore, for the upflow, as observed experimentally, no liquid region passes through the top end of this packed column. The thickness of the two-phase region increases monotonically with increase in x_F^*, because the capillary force becomes dominant as u_F^* decreases. As shown in Fig. 10, the location of first and second transition, $x_{tr,1}^*$ and $x_{tr,2}^*$, are proportional to 1.28 and 1.78 power of p_0^*, respectively. The first transition point $x_{tr,1}^*$ is independent of Ja, while $x_{tr,2}^*$ increases with Ja and this has a dependency to a power of 1.26. The distance between $x_{tr,1}^*$ and $x_{tr,2}^*$ decreases with the decrease in p_0^* and then disappears when $p_0^* < 4.2$, for $Ja = 0.117$.

Figure 11 shows the predicted and measured variation of u_F^*/Bo with respect to $x_F^* Ja/p_0^*$ for the upflow and downflow, where the inlet pressure in the experiment corresponds to that presented in Fig. 4. As observed in Fig. 11, u_F^*/Bo is a function of the newly scaled location, i.e. $x_F^* Ja/p_0^*$.

For the downflow, the asymptotes for $x_F^* Ja/p_0^* \to 0$ and ∞ correspond to the Darcean and non-Darcean

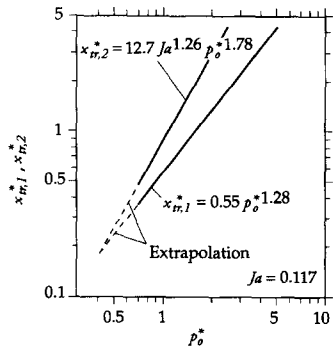

Fig. 10. Predicted variations of location of the transition from a discontinuous irreducible to a continuous immobile liquid saturation (the first transition, $x_{tr,1}^*$) and location marking the disappearance of the liquid region (the second transition, $x_{tr,2}^*$).

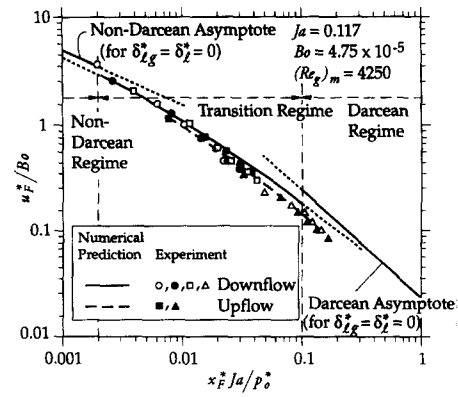

Fig. 11. Predicted and measured variations of the normalized front speed with respect to the scaled front location for the up- and downflow and for several inlet pressures. The Darcean and non-Darcean asymptotes are also shown.

(or far-field and near-field) regimes, respectively. For these the conditions of $\delta_{lg}^* = \delta_l^* = 0$ are imposed and the Darcean and non-Darcean asymptotes are found. For the Darcean to non-Darcean transition regime, using a second-order equation for u_F^*/Bo, a curve fitted correlation is found. Then we have

$$\frac{u_F^*}{Bo} = \begin{cases} \dfrac{1}{C_1\left(\dfrac{x_F^* Ja}{p_0^*}\right)} & 0.1 < \dfrac{x_F^* Ja}{p_0^*} \\ \text{Darcean regime} & \\ \dfrac{-a_1 + \left[a_1^2 + \dfrac{4a_2 C_2}{\left(\dfrac{x_F^* Ja}{p_0^*}\right)}\right]^{1/2}}{2a_2 C_1 C_2} & 0.002 < \dfrac{x_F^* Ja}{p_0^*} < 0.1 \\ \text{transition regime} & \\ \dfrac{1}{C_1 C_2\left(\dfrac{x_F^* Ja}{p_0^*}\right)^{1/2}} & \dfrac{x_F^* Ja}{p_0^*} < 0.002 \\ \text{non-Darcean regime,} & \end{cases} \tag{37}$$

where

$$C_1 = \frac{\rho^*(1-\varepsilon)}{\mu^*} \quad C_2 = \left[\frac{C_E}{(1-s_{ir})^6}(Re_g)_m Bo\, Ja\right]^{1/2}$$

$$(Re_g)_m = \frac{(\sigma/\mu_g)\rho_g K^{1/2}}{\mu_g} \quad a_1 = 1.16 \quad a_2 = 6.56. \tag{38}$$

In equation (37), u_F^*/Bo is inversely proportional to $x_F^* Ja/p_0^*$ in the Darcean regime, while it varies with a -0.5 power of $x_F^* Ja/p_0^*$ and with $(Re_g)_m Bo\, Ja$ in the transition and non-Darcean regimes. As shown in Fig.

11, for low inlet pressures there is a small deviation from the correlation in the transition regime.

For the upflow, as $x_F^* Ja/p_0^* \to 0$, u_F^*/Bo approaches the results for the downflow. In the Darcean regime, u_F^*/Bo is below the asymptotic value, because of the decrease in the relative permeabilities (by the continuous, immobile liquid saturation s_{im}) in the upstream region. Although not attempted, it is possible to seek a correlation for the upflow by including inverse functions of the third and sixth powers of s_{im} in the viscous and inertial terms, respectively.

5. SUMMARY

Under a constant injection pressure for one-dimensional steam flow into a lower temperature, dry porous medium, the condensation-front speed and liquid saturation distribution in the condensate region have been examined theoretically. A quasi-steady behavior is assumed, and the existing models are used for the volumetric viscous and inertial forces. Four different regions and a condensation zone are defined. The dimensionless system parameters of the problems are Ja, Bo, p_0^*, and the scaled thermophysical properties. The dimensionless front speed u_F^* or the front location x_F^* are found for the down- and upflow of steam.

For the downflow, a liquid region is present and increases in thickness with the distance from the entrance. The steam flow rate is initially high, and, therefore, the deviation from the Darcean flow behavior is significant for this initial period (or for the region affected during this period). For the upflow, the liquid region gradually disappears, and the upstream region will contain a transition from a discontinuous to a continuous but immobile liquid saturation. The experiments confirmed these predictions for the upward and downward flows.

For the downward flow, the front speed is found in a closed form as a function of the distance from the entrance for the Darcean (far-field) and non-Darcean (near-field) regimes and correlated for the transitional regime. For the upflow, the location of transition from the irreducible to immobile liquid saturations and the location of the disappearance of the liquid region are also correlated as functions of the dimensionless system parameters.

Acknowledgment—The financial support of the National Science Foundation through grant CTS-91-15746 is greatly appreciated.

REFERENCES

1. G. Mandl and C. W. Volek, Heat and mass transport in steam-drive processes, *SPE J. Trans. AIME* **246**, 59–79 (1969).
2. Y. C. Yortsos and G. R. Gavalas, Analytical modeling of oil recovery by steam injection: Part 1—upper bounds, *SPE J.* 162–178 (1981).
3. Y. C. Yortsos and G. R. Gavalas, Analytical modeling of oil recovery by steam injection: Part 2—asymptotic and approximate solutions, *SPE J.* 179–190 (1981).
4. J. R. Hunt, N. Sitar and K. S. Udell, Nonaqueous phase liquid transport and cleanup 1. Analysis of mechanisms, *Water Resour. Res.* **24**, 1247–1258 (1988).
5. J. R. Hunt, N. Sitar and K. S. Udell, Nonaqueous phase liquid transport and cleanup 2. Experimental studies, *Water Resour. Res.* **24**, 1259–1269 (1988).
6. D. K. Menegus and K. S. Udell, A study of steam injection into water saturated capillary porous media. In *Heat Transfer in Porous Media and Particulate Flows*, HTD-Vol. 46, pp. 151–157. ASME, New York (1985).
7. L. D. Stewart, M. D. Basel and K. S. Udell, The effect of gravity on steam propagation in porous media. In *Multiphase Transport in Porous Media*, HTD-Vol. 91, pp. 31–42. ASME, New York (1989).
8. L. D. Stewart and K. S. Udell, Mechanisms of residual oil displacement by steam injection, *SPE Reserv. Engng* 1233–1242 (1988).
9. P. F. Ahner and A. H. Sufi, Physical model steamflood studies using horizontal wells, SPE/DOE paper no. 20247, pp. 717–728 (1990).
10. M. Kaviany, *Principles of Heat Transfer in Porous Media*. Springer, New York (1991).
11. J. Bear, *Dynamics of Fluids in Porous Medium*. Dover, New York (1985).
12. R. Krupiczka, Analysis of thermal conductivity in granular materials, *Int. Chem. Engng* **7**, 122–144 (1967).
13. F. P. Incropera and D. P. Dewitt, *Introduction to Heat Transfer*. Wiley, New York (1985).